Supplement of Atmos. Chem. Phys., 20, 14063–14075, 2020
https://doi.org/10.5194/acp-20-14063-2020-supplement

Atmospheric Chemistry and Physics
Open Access

Supplement of

Impact of in-cloud aqueous processes on the chemical compositions and morphology of individual atmospheric aerosols

Yuzhen Fu et al.

Correspondence to: Guohua Zhang (zhanggh@gig.ac.cn) and Xinhui Bi (bixh@gig.ac.cn)

1 Air mass backward trajectories and meteorology conditions

The backward trajectory and the height (above sea level) of air masses during sampling were calculated by the Hybrid Single Particle Lagrangian Integrated Trajectory (HYSPLIT) model (http://ready.arl.noaa.gov). During three cloud events, the sampling site was greatly influenced by air masses from Southeast Asia, northern China and the South China Sea. Compared with the cloud event #1, the air masses of cloud event #2 and #3 passed through a relatively low path on the way to the sampling site. Thus, the air masses of cloud event #2 and #3 were affected more by the ground anthropogenic emissions. The ambient temperature at the sampling station varied from 12.1 to 18.6 °C during three cloud events. All samples were collected during the stable period of cloud events, when the mass concentration of $PM_{2.5}$ was less than 5 μg m^{-3} and visibility was less than 100 m. The concentrations of $PM_{2.5}$ during cloud event #1 were lower than those during cloud event #2 and #3. Consistently, the mean concentrations of O_3, SO_2 and NO_X were higher in the cloud event #2 and #3 (Table S1).

2 The size distribution of RES and INT

In this study, a $PM_{2.5}$ cyclone inlet and a GCVI (ground-based counterflow virtual impactor) inlet were used to collect INT and RES, which is similar to Cozic et al. (2007). Additionally, the particle size in this study refers to as ECD (equivalent circle diameter) obtained from TEM images, which is larger than ESD (equivalent spherical diameter). Liu et al. (2018) showed that the ECD of individual dry particles on the substrate is 0.4952 times that of the ESD.

The size distribution data shows a higher median diameter of RES (1.20 μm) than INT (0.63 μm) (Figure S2), which are higher than those (0.8 and 0.45 μm, respectively) at Mount Tai in northern China (Li et al., 2011). This could be because Mount Tai is located in an industrial area, whereas our site represents a background region mainly influenced by long-range transport. Additionally, the formation of secondary compounds during cloud events increases the size of RES (Zhang et al., 2017).

The size distribution of different particle types revealed that S-rich and aged soot particles were predominant in smaller size segments, and aged mixture particles in larger size segments (Figure S8). Likewise, the size-resolved number fractions of different particle types from the results of the SPAMS also showed that the BC-containing particles were mainly distributed between 0.1 and 1.3 μm, representing ~80% of the submicron RES and ~73% of the submicron INT population, respectively (Figure S9).

3 Identification of several types of particles within RES and INT measured by SPAMS

The information on particle sizes and mass spectra is imported into the Matlab for subsequent analysis using the FATES toolkit (Sultana et al., 2017). A total of 117,436 particles from the SPAMS were analyzed. All the particles with bipolar mass spectra and the size range of d_{va} 0.1–1.9 μm were classified several clusters by an adaptive resonance theory neural network (ART-2a) with a learning rate of 0.05, a vigilance factor of 0.8 and 20 iterations, and merged similar clusters manually. Ten characteristic particle types (Figure S1) were obtained, including BC (black carbon)-containing, OC (organic carbon), HMOC (highly molecular organic carbon), Dust, K-rich, Metal, Na-K, Amines, SS (sea salt) and Others. BC-containing particles are characterized by elemental carbon cluster ions (*m/z* $12C^{\pm}$, $24C_2^{\pm}$, $36C_3^{\pm}$, $48C_4^{\pm}$, …) (Arndt et al., 2017). OC particles mainly contain fragment ions of organics (*m/z* $27C_2H_3^+$, $37C_3H^+$, $43C_2H_3O^+$, $-26CN^-$, …) (Denkenberger et al., 2007; Qin et al., 2012). The mass spectra of HMOC particles show the presence of peaks of OC particles and some other organic peaks (such as *m/z* $77C_6H_5^+$, $91C_7H_7^+$). Furthermore, HMOC particles are distinguished from OC particles by marked ion fragments detected in range of *m/z* > 100 (Qin and Prather, 2006). Dust particles present significant ions at *m/z* $27Al^+$, $40Ca^+$ and $56CaO^+/Fe^+$ (Silva et al., 2000). K-rich particles are identified according to the strong signal at *m/z* $39K^+$ only in positive mass spectra. Metal particles show the presence of metal ion peaks (such as Fe^+ (*m/z* 54 and 56), Mn^+ (*m/z* 55), Pb^+ (*m/z* 206, 207 and 208)) in positive mass spectra. Na-K particles are characterized by peaks at *m/z* $23Na^+$, $39K^+$, and less intense peaks at *m/z* $-46NO_2^-$, $-62NO_3^-$, $-97HSO_4^-$. The mass spectra of amines particles contain ions signals at *m/z* $59N(CH_3)_3^+$, $86C_5H_{12}N^+$, $101C_6H_{15}N^+$ (Angelino et al., 2001; Pratt et al., 2009). SS particles are mainly composed of ions peaks at *m/z* $23Na^+$, $46Na_2^+$, $62Na_2O^+$, $63Na_2OH^+$ and $81Na_2Cl^+$ (Gaston et al., 2011). Most particles are observed to be internally mixed with sulfate and nitrate (*m/z* -46, -62, -97). Particles with inconspicuous mass spectrum characteristics are named as others. Specific classification criteria were described in detail elsewhere (Zhang et al., 2015).

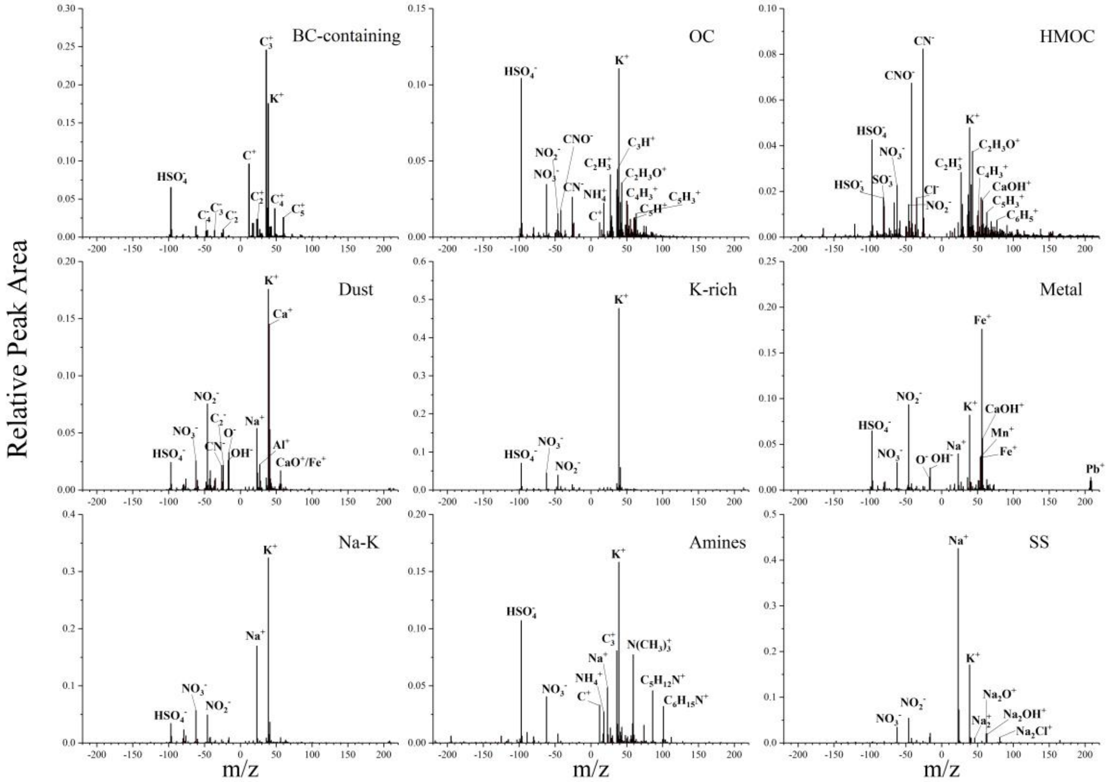

Figure S1. Average positive and negative mass spectra of the main particle types (i.e., BC-containing, OC, HMOC, Dust, K-rich, Metal, Na-K, Amines, SS) measured by SPAMS.

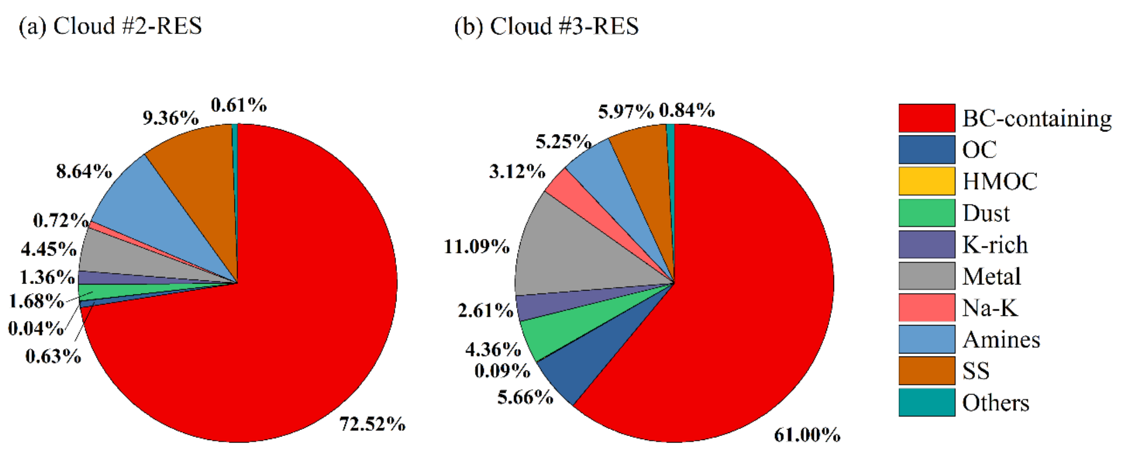

Figure S2. The chemical composition of RES measured by the SPAMS during cloud event #2 and #3.

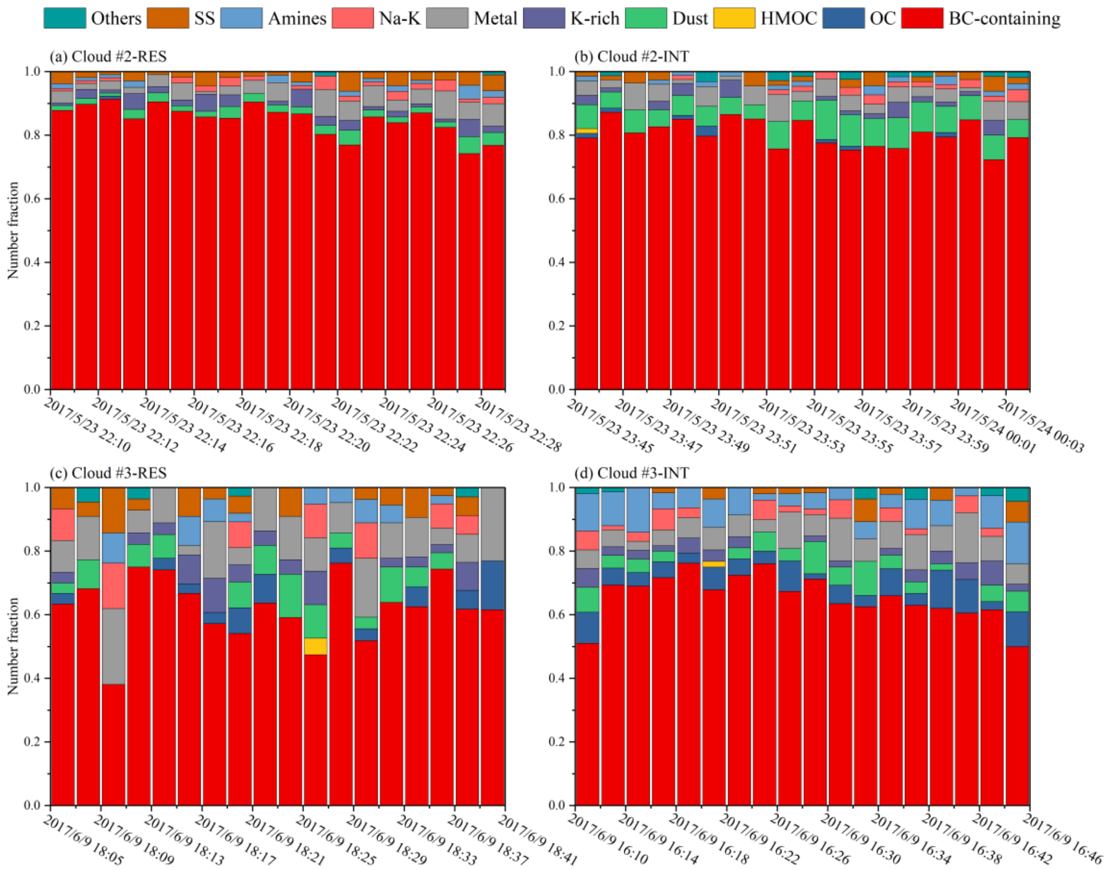

Figure S3. Time series of the chemical composition of RES and INT measured by the SPAMS during cloud events #2 and #3.

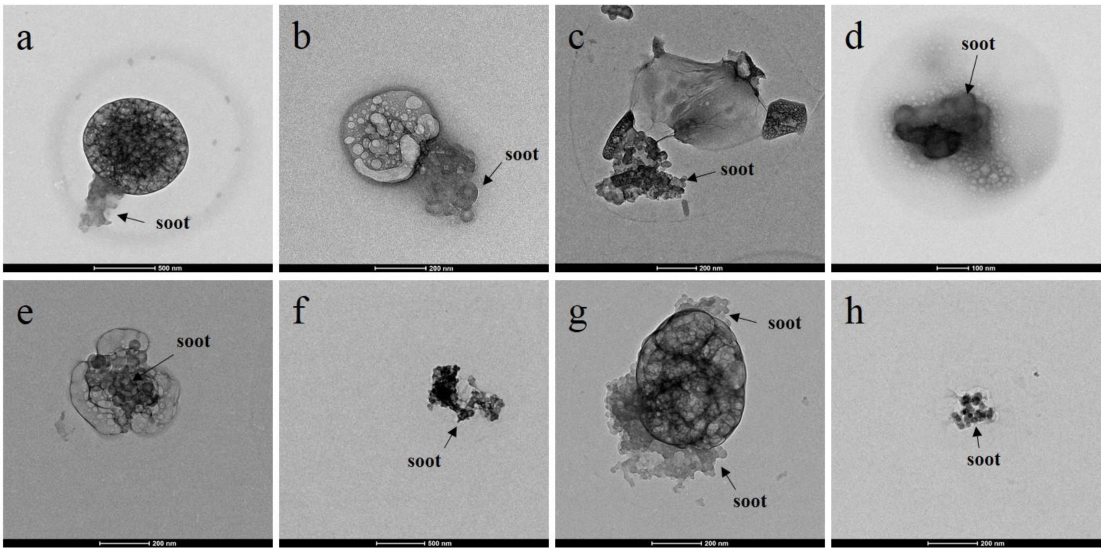

Figure S4. Typical TEM images of soot particles in the RES (a-d) and INT (e-h).

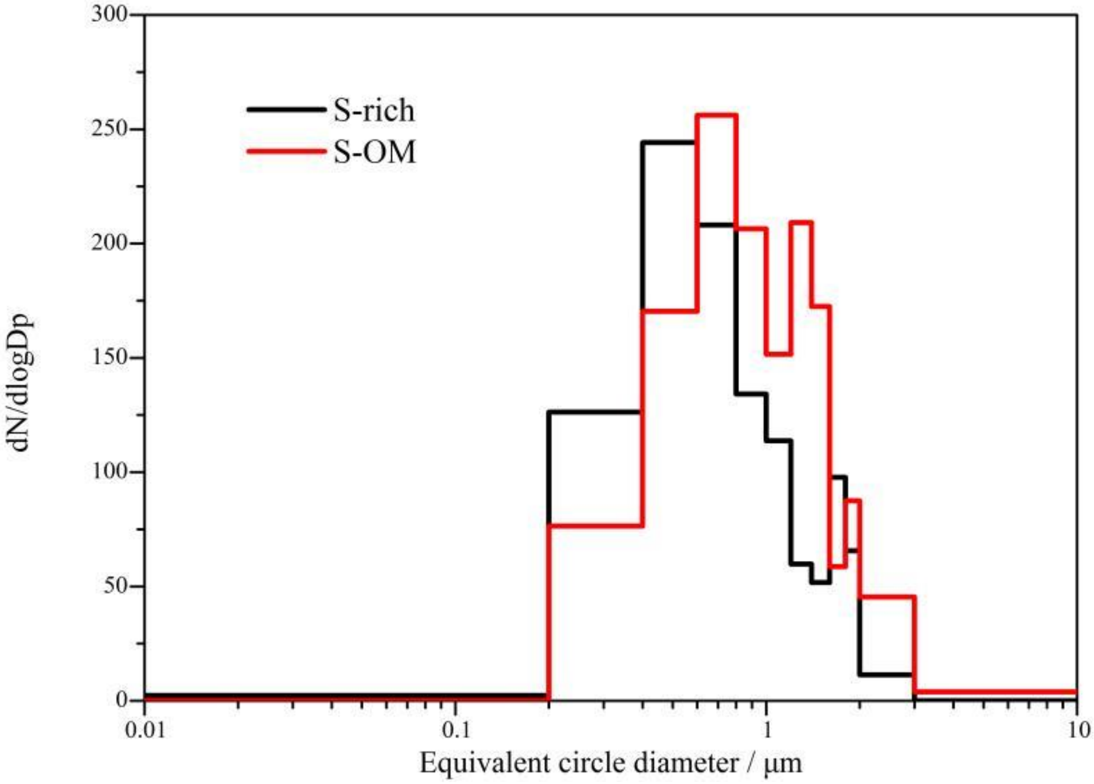

Figure S5. The size distribution of S-rich and S-OM particles. There are few S-rich particles with the size of less than 0.2 μm, and the median size are 0.56 μm and 0.76 μm for S-rich and S-OM particles, respectively.

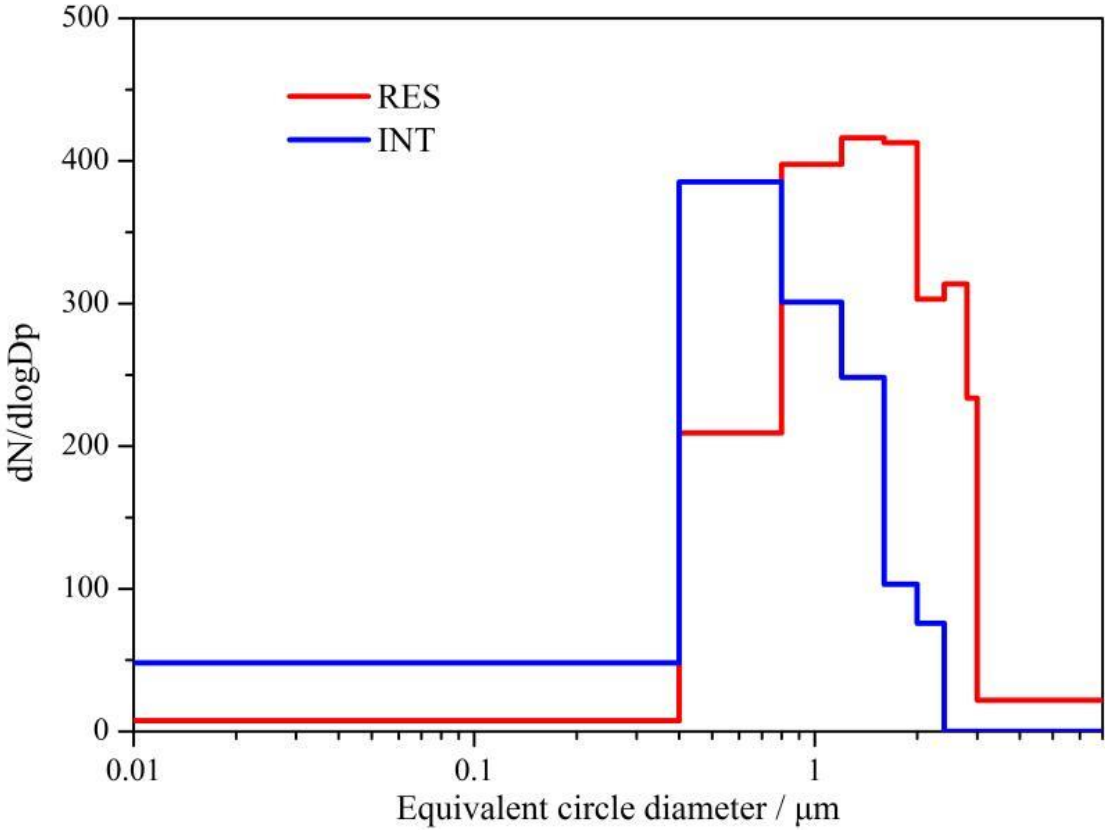

Figure S6. Size distribution of RES and INT during cloud event #2 and #3. There are more INT particles when the size is less than 0.8 μm, and more RES particles when the size is larger than 0.8 μm.

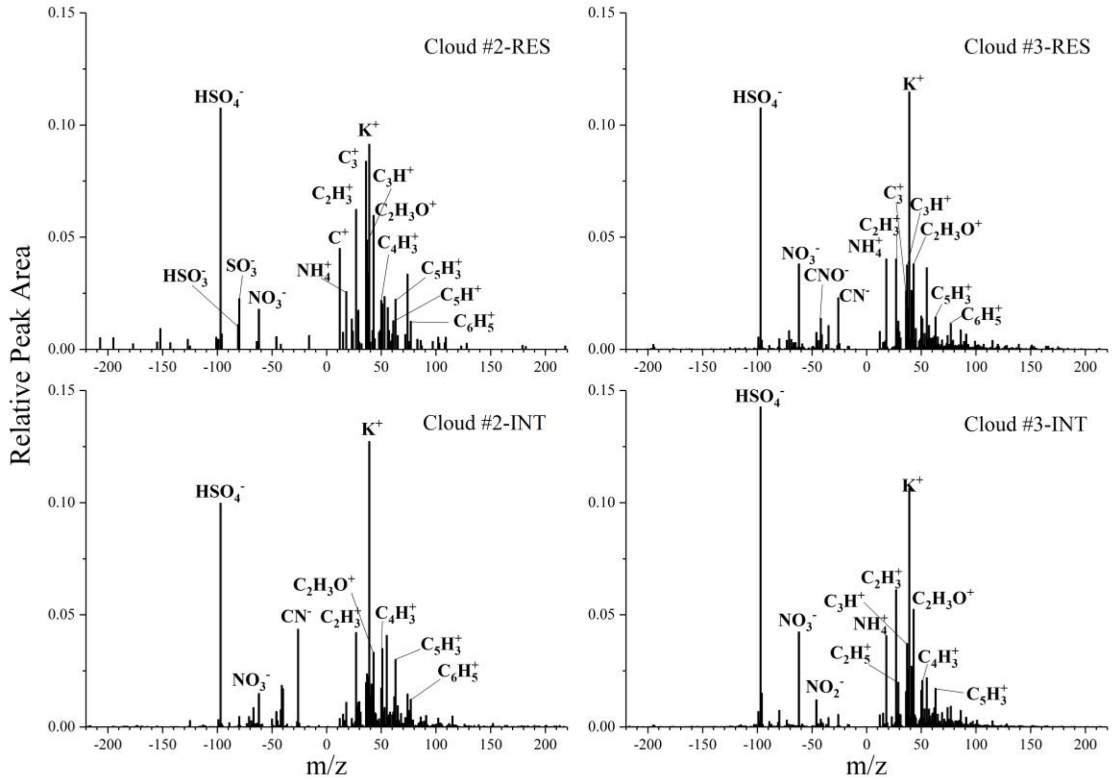

Figure S7. Average positive and negative mass spectra of OM particles (OC and HMOC) of RES and INT particles measured by the SPAMS during cloud events #2 and #3.

73

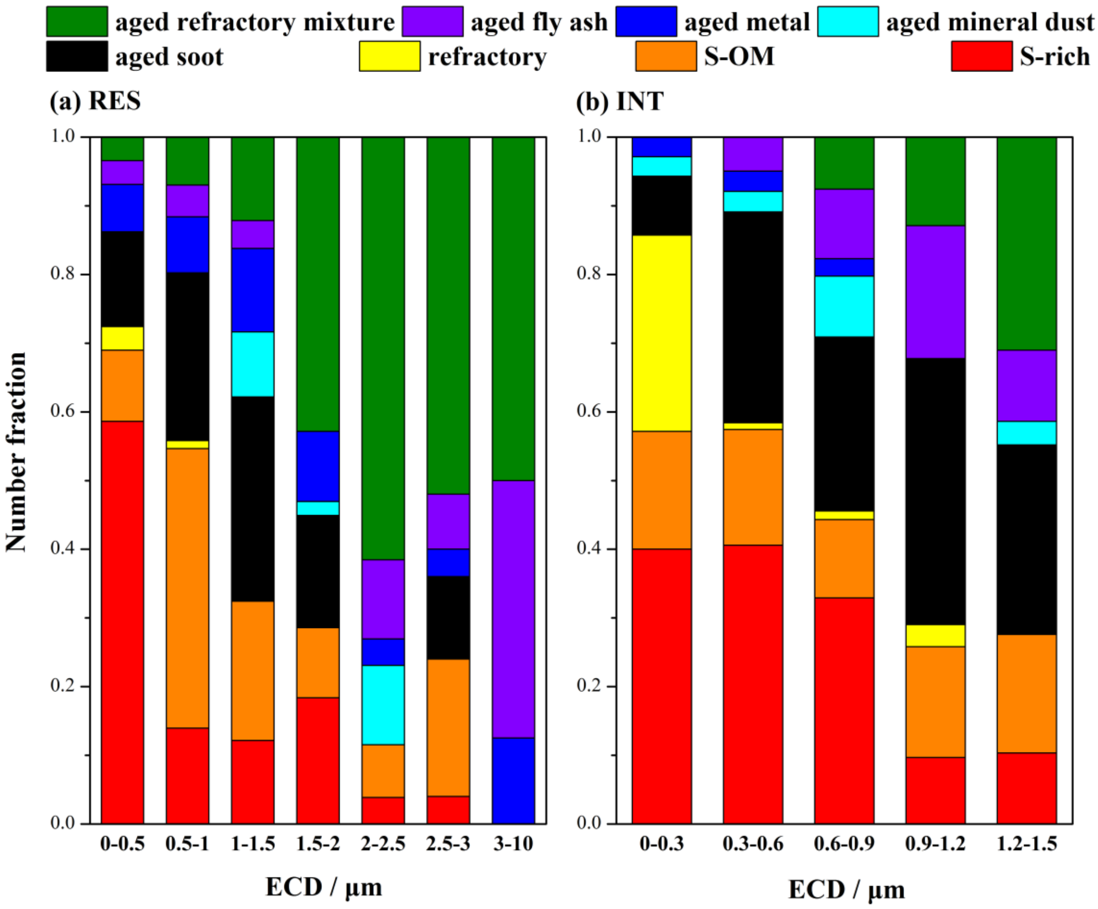

74 **Figure S8. Size-resolved number fraction distributions of RES and INT by TEM/EDS.**

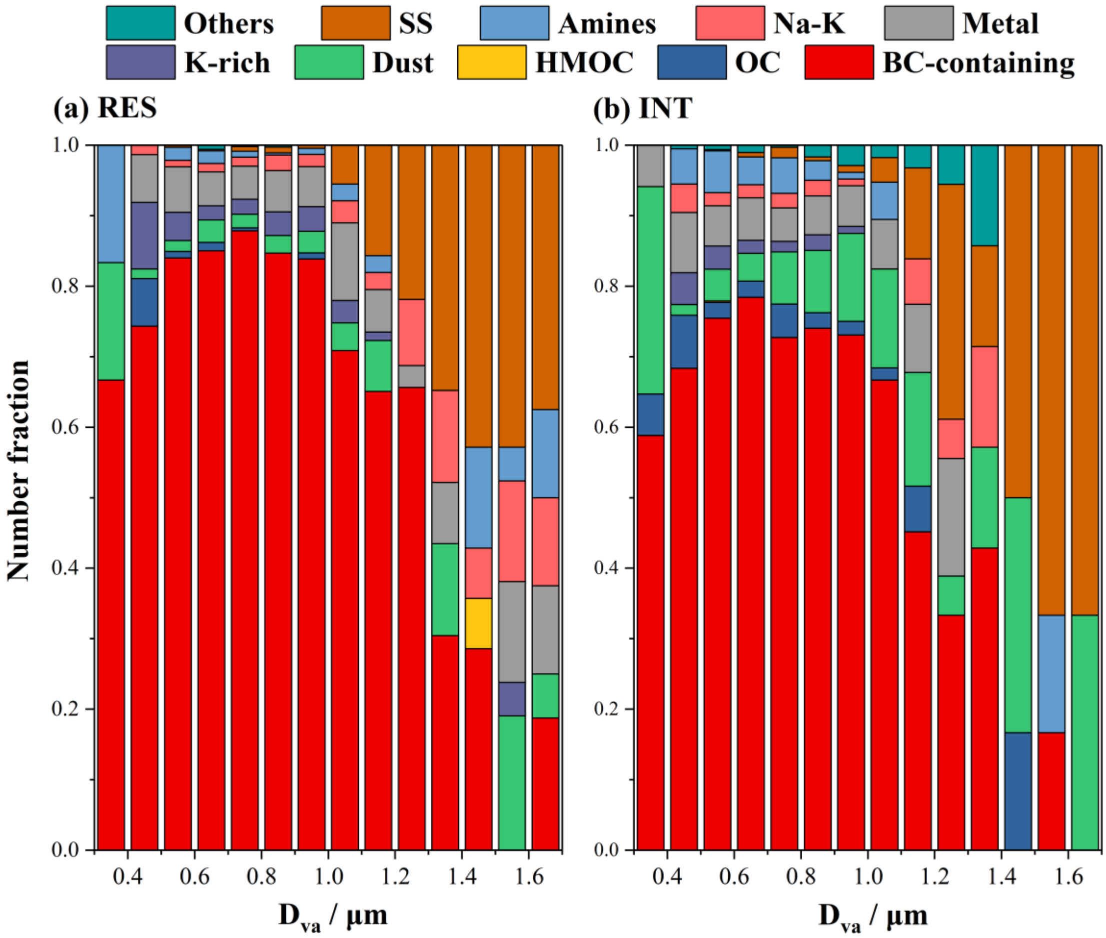

Figure S9. Size-resolved number fraction distributions of RES and INT by the SPAMS.

Table S1. The concentration of NO_X, SO_2, O_3, PM_{10} and $PM_{2.5}$ during three cloud events.

cloud event	NO_X (ppb)	SO_2 (ppb)	O_3 (ppb)	PM_{10} (μg m^{-3})	$PM_{2.5}$ (μg m^{-3})
#1	2.6	0.4	30.5	3.6	1.1
#2	3.5	1.2	39.1	4.8	1.9
#3	4.3	0.6	34.4	11.4	4.7

Table S2. The ratios of relative peak area between organics (*m/z* 27, 29, 37, 43, 50, 51, 61, 63) and sulfate (*m/z* -97) of OM particles (OC and HMOC) during in-cloud (RES and INT) and pre-cloud (Ambient) periods.

	RES	INT	Ambient
Organics/Sulfates	1.68	1.57	1.59

Table S3. Morphological descriptors of soot particles within RES and INT.

parameters	A_p	d_p	L_{max}	N	D_f	k_g
RES	1658(175)	43(2)	255(12)	66(8)	1.82(0.12)	3.5(0.08)
INT	1842(133)	46(2)	316(16)	68(6)	2.11(0.09)	2.72(0.05)

A_p, mean projected area of the monomer; d_p, monomer diameter; L_{max}, maximum length of soot aggregates; N, number of monomers in a soot aggregate; D_f, mass fractal dimension; k_g, structural coefficient. In parentheses are the standard error of A_p, d_p, L_{max}, N, D_f and k_g.

Table S4. Overlap (δ), constant (k_a) and empirical exponent (α).

parameters	δ	k_a	α
RES	1.54	1.52	1.13
INT	1.4	1.44	1.11

References

Angelino, S., Suess, D. T., and Prather, K. A.: Formation of aerosol particles from reactions of secondary and tertiary alkylamines: Characterization by aerosol time-of-flight mass spectrometry, Environmental Science & Technology, 35, 3130-3138, 10.1021/es0015444, 2001.

Arndt, J., Sciare, J., Mallet, M., Roberts, G. C., Marchand, N., Sartelet, K., Sellegri, K., Dulac, F., Healy, R. M., and Wenger, J. C.: Sources and mixing state of summertime background aerosol in the north-western Mediterranean basin, Atmospheric Chemistry and Physics, 17, 6975-7001, 10.5194/acp-17-6975-2017, 2017.

Cozic, J., Verheggen, B., Mertes, S., Connolly, P., Bower, K., Petzold, A., Baltensperger, U., and Weingartner, E.: Scavenging of black carbon in mixed phase clouds at the high alpine site Jungfraujoch, Atmospheric Chemistry and Physics, 7, 1797-1807, 10.5194/acp-7-1797-2007, 2007.

Denkenberger, K. A., Moffet, R. C., Holecek, J. C., Rebotier, T. P., and Prather, K. A.: Real-time, single-particle measurements of oligomers in aged ambient aerosol particles, Environmental Science & Technology, 41, 5439-5446, 10.1021/es070329l, 2007.

Gaston, C. J., Furutani, H., Guazzotti, S. A., Coffee, K. R., Bates, T. S., Quinn, P. K., Aluwihare, L. I., Mitchell, B. G., and Prather, K. A.: Unique ocean-derived particles serve as a proxy for changes in ocean chemistry, Journal of Geophysical Research-Atmospheres, 116, D18310, 10.1029/2010jd015289, 2011.

Liu, L., Zhang, J., Xu, L., Yuan, Q., Huang, D., Chen, J., Shi, Z., Sun, Y., Fu, P., Wang, Z., Zhang, D., and Li, W.: Cloud scavenging of anthropogenic refractory particles at a mountain site in North China, Atmospheric Chemistry and Physics, 18, 14681-14693, 10.5194/acp-18-14681-2018, 2018.

Li, W., Li, P., Sun, G., Zhou, S., Yuan, Q., and Wang, W.: Cloud residues and interstitial aerosols from non-precipitating clouds over an industrial and urban area in northern China, Atmospheric Environment, 45, 2488-2495, 10.1016/j.atmosenv.2011.02.044, 2011.

Pratt, K. A., Hatch, L. E., and Prather, K. A.: Seasonal Volatility Dependence of Ambient Particle Phase Amines, Environmental Science & Technology, 43, 5276-5281, 10.1021/es803189n, 2009.

Qin, X., and Prather, K. A.: Impact of biomass emissions on particle chemistry during the California Regional Particulate Air Quality Study, International Journal of Mass Spectrometry, 258, 142-150, 10.1016/j.ijms.2006.09.004, 2006.

Qin, X., Pratt, K. A., Shields, L. G., Toner, S. M., and Prather, K. A.: Seasonal comparisons of single-particle chemical mixing state in Riverside, CA, Atmospheric Environment, 59, 587-596, 10.1016/j.atmosenv.2012.05.032, 2012.

Silva, P. J., Carlin, R. A., and Prather, K. A.: Single particle analysis of suspended soil dust from Southern California, Atmospheric Environment, 34, 1811-1820, 10.1016/s1352-2310(99)00338-6, 2000.

Sultana, C. M., Cornwell, G. C., Rodriguez, P., and Prather, K. A.: FATES: a flexible analysis toolkit for the exploration of single-particle mass spectrometer data, Atmos. Meas. Tech., 10, 1323-1334, doi:10.5194/amt-10-1323-2017, 2017.

Zhang, G., Han, B., Bi, X., Dai, S., Huang, W., Chen, D., Wang, X., Sheng, G., Fu, J., and Zhou, Z.: Characteristics of individual particles in the atmosphere of Guangzhou by single particle mass spectrometry, Atmospheric Research, 153, 286-295, 10.1016/j.atmosres.2014.08.016, 2015.

Zhang, G., Lin, Q., Peng, L., Bi, X., Chen, D., Li, M., Li, L., Brechtel, F. J., Chen, J., Yan, W., Wang, X., Peng, P., Sheng, G., and Zhou, Z.: The single-particle mixing state and cloud scavenging of black carbon: a case study at a high-altitude mountain site in southern China, Atmospheric Chemistry and Physics, 17, 14975-14985, 10.5194/acp-17-14975-2017, 2017.